



**SYNTHESIS AND CHARACTERISATION OF  
TERNARY SYSTEM  $\text{LiCoPO}_4\text{-LiNiPO}_4\text{-LiMnPO}_4$   
CATHODE MATERIALS FOR Li-ION BATTERIES**

by

**TAN TZE QING  
(1540411725)**

A thesis submitted in fulfillment of the requirements for the degree of  
Doctor of Philosophy

**School of Materials Engineering  
UNIVERSITI MALAYSIA PERLIS**

2018

## ACKNOWLEDGMENT

This thesis was the outcome of years of research that has been done since I first joined Centre for Frontier Materials Research group. Over these years, a great number of people have contributed in this research expedition.

First and foremost, I would like to devote deepest and sincere gratitude to my main supervisor Dr. Mohd Sobri Idris for his constant guidance, critical judgement and commitment throughout the whole period of my PhD research studies. He has been a great mentor who always like to share his knowledge especially in the field of X-ray diffraction and Rietveld refinement. I am very grateful for his patience and continuous encouragement given during the learning process. I am also very thankful for the valuable knowledge and experience that were shared by Dr. Rozana Aina Maulat Osman (UniMAP) and Dr. M. V. Venkatasamy Reddy (National University of Singapore).

I have been extremely blessed with good fortune to have the opportunity to come to a lab each day and be greeted by friendly, charismatic and insightful group of people who provide support and enthusiasm over the many years of my studies. Hearty thanks to every members of the Centre of Excellence for Frontier Materials Research, in particular, to Mrs. Wan Masku, Mrs. Najwa Shafiqah, Mrs. Nurhamidah, Ms. Fatin Adila, Ms. Tuan Amirah, Ms. Norhizatol Fashreen, Mrs. Ku Noor Dhaniah and lab technician, Mr. Mohammed Faisal Rusli who have contributed in different ways throughout my doctoral degree.

In addition, I am thankful to the Ministry of Higher Education (MOHE) Malaysia for funding this project through the Fundamental Research Grant Scheme 2014 (FRGS Grant No.: FRGS/1/2014/TK06/UNIMAP/02/5) and the scholarship (MyBrain15-MyPhD) which financially aided my doctoral degree studies.

On top of that, I am overwhelmed with gratitude for the encouragement, support, love and tolerance from my family members for giving me the strength to complete my research project. My deepest gratitude goes to my wonderful husband, Mr. Lim Kim Hock for his unequivocally support during my PhD study.

## TABLE OF CONTENTS

	<b>PAGE</b>
<b>DECLARATION OF THESIS</b>	<b>i</b>
<b>ACKNOWLEDGMENT</b>	<b>ii</b>
<b>TABLE OF CONTENTS</b>	<b>iii</b>
<b>LIST OF TABLES</b>	<b>vii</b>
<b>LIST OF FIGURES</b>	<b>x</b>
<b>LIST OF ABBREVIATIONS</b>	<b>xvi</b>
<b>LIST OF SYMBOLS</b>	<b>xvii</b>
<b>LIST OF EQUATIONS</b>	<b>xviii</b>
<b>ABSTRAK</b>	<b>xx</b>
<b>ABSTRACT</b>	<b>xxi</b>
<b>CHAPTER 1 : INTRODUCTION</b>	<b>1</b>
1.1 Background	1
1.1.1 Basic Operating Principle of Li-ion Batteries	3
1.1.2 Negative Electrodes (Anodes)	5
1.1.3 Positive Electrodes (Cathodes)	9
1.1.4 Electrolytes	11
1.2 Problem Statement	12
1.3 Objectives	15
1.4 Scope of Study	16
1.5 Thesis Structure	17
1.6 Novelty of Research Findings	18
<b>CHAPTER 2 : LITERATURE REVIEW</b>	<b>19</b>
2.1 Overview	19

2.2	Crystal Structure of Cathode Materials	19
2.3	Cathode Materials with Layered Rock Salt Structure	25
2.3.1	Layered $\text{LiMO}_2$ Compounds ( $M = \text{Co, Ni, Mn, and etc.}$ )	25
2.3.2	Role of Cation Mixing in Layered Rock Salt Structure Materials	27
2.4	Cathode Materials with Spinel Structure	29
2.4.1	Spinel $\text{LiMn}_2\text{O}_4$ Compound and Its Analogous	29
2.4.2	Role of Cation Order-disorder in Spinel Structure Materials	33
2.5	Cathode Materials with Olivine Structure	35
2.5.1	Olivine $\text{LiMPO}_4$ Compounds ( $M = \text{Fe, Mn, Ni, Co}$ )	35
2.5.2	Role of Anti-site Defects in Olivine Structure Materials	50
<b>CHAPTER 3 : RESEARCH METHODOLOGY</b>		<b>52</b>
3.1	Introduction	52
3.2	Materials Synthesis	52
3.2.1	Raw Materials	53
3.2.2	Conventional Solid State Reaction	54
3.3	Materials Characterisation	57
3.3.1	Powder X-ray Diffraction (XRD) and Bragg's Law	58
3.3.2	Structure Refinement (Rietveld Refinement)	62
3.3.3	Scanning Electron Microscopy	65
3.3.4	Impedance Spectroscopy	66
3.3.5	Electrochemical Characterisation	69
<b>CHAPTER 4 : RESULTS &amp; DISCUSSION</b>		<b>74</b>
4.1	Introduction	74
4.2	End members of phase triangle, $\text{LiMPO}_4$ ( $M = \text{Mn, Co, Ni}$ )	74
4.2.1	Structural analysis of $\text{LiCoPO}_4$ as a function of temperature	75
4.2.2	Structural comparison of $\text{LiMPO}_4$ ( $M = \text{Mn, Co, Ni}$ )	78
4.2.3	Electrical analysis of $\text{LiMPO}_4$ ( $M = \text{Mn, Co, Ni}$ )	83

4.2.4	Microstructural comparison of $\text{LiMPO}_4$ ( $M = \text{Mn, Co, Ni}$ )	85
4.2.5	Summary	86
4.3	Complex olivine $\text{LiCo}_{1-x}[\text{Ni}_{0.5}\text{Mn}_{0.5}]_x\text{PO}_4$ ( $0 \leq x \leq 1$ )	87
4.3.1	Structural analysis of $\text{LiCo}_{1-x}[\text{Ni}_{0.5}\text{Mn}_{0.5}]_x\text{PO}_4$ ( $0 \leq x \leq 1$ ) at 1000 °C: comparison between slow-cooled and quenched samples	87
4.3.2	Electrical analysis of $\text{LiCo}_{1-x}[\text{Ni}_{0.5}\text{Mn}_{0.5}]_x\text{PO}_4$ ( $0 \leq x \leq 1$ ) at 1000 °C: comparison between slow-cooled and quenched samples	95
4.3.3	Microstructural analysis of $\text{LiCo}_{1-x}[\text{Ni}_{0.5}\text{Mn}_{0.5}]_x\text{PO}_4$ ( $0 \leq x \leq 1$ ) at 1000 °C	100
4.3.4	Summary	102
4.4	Complex olivine $\text{LiNi}_{1-x}[\text{Co}_{0.5}\text{Mn}_{0.5}]_x\text{PO}_4$ ( $0 \leq x \leq 1$ )	103
4.4.1	Structural analysis of $\text{LiNi}_{1-x}[\text{Co}_{0.5}\text{Mn}_{0.5}]_x\text{PO}_4$ ( $0 \leq x \leq 1$ ) at 1000 °C: comparison between slow-cooled and quenched samples	104
4.4.2	Electrical analysis of $\text{LiNi}_{1-x}[\text{Co}_{0.5}\text{Mn}_{0.5}]_x\text{PO}_4$ ( $0 \leq x \leq 0.8$ ) at 1000 °C: comparison between slow-cooled and quenched samples	114
4.4.3	Microstructural analysis of $\text{LiNi}_{1-x}[\text{Co}_{0.5}\text{Mn}_{0.5}]_x\text{PO}_4$ ( $0 \leq x \leq 1$ ) at 1000 °C	119
4.4.4	Summary	121
4.5	Complex olivine $\text{LiMn}_{1-x}[\text{Co}_{0.5}\text{Ni}_{0.5}]_x\text{PO}_4$ ( $0 \leq x \leq 1$ )	122
4.5.1	Structural analysis of $\text{LiMn}_{1-x}[\text{Co}_{0.5}\text{Ni}_{0.5}]_x\text{PO}_4$ ( $0 \leq x \leq 1$ ) at 1000 °C: comparison between slow-cooled and quenched samples	122
4.5.2	Electrical analysis of $\text{LiMn}_{1-x}[\text{Co}_{0.5}\text{Ni}_{0.5}]_x\text{PO}_4$ ( $0 \leq x \leq 1$ ) at 1000 °C: comparison between slow-cooled and quenched samples	130
4.5.3	Microstructural analysis of $\text{LiMn}_{1-x}[\text{Co}_{0.5}\text{Ni}_{0.5}]_x\text{PO}_4$ ( $0 \leq x \leq 1$ ) at 1000 °C	133
4.5.4	Summary	135
4.6	Complex olivine $\text{LiNi}_{1/3}\text{Mn}_{1/3}\text{Co}_{1/3}\text{PO}_4$	136
4.6.1	Structural analysis as a function of temperature	137

4.6.2	Electrical analysis as a function of temperature	140
4.6.3	Microstructural analysis as a function of temperature	142
4.6.4	Investigation of the effects of ball milling time on the crystallite sizes	143
4.6.5	Evaluation of the effect of different conductive carbon	148
4.6.6	Summary	152
4.7	Spinel Zn doped $\text{Li}_2\text{CoMn}_3\text{O}_8$ ( $\text{Li}_2\text{Co}_{1-x}\text{Zn}_x\text{Mn}_3\text{O}_8$ ) ( $0 \leq x \leq 1$ )	153
4.7.1	Structural analysis of $\text{Li}_2\text{Co}_{1-x}\text{Zn}_x\text{Mn}_3\text{O}_8$ ( $0 \leq x \leq 1$ )	153
4.7.2	Microstructural analysis of $\text{Li}_2\text{Co}_{1-x}\text{Zn}_x\text{Mn}_3\text{O}_8$ ( $0 \leq x \leq 1$ )	156
4.7.3	Electrochemical properties of $\text{Li}_2\text{Co}_{1-x}\text{Zn}_x\text{Mn}_3\text{O}_8$ ( $0 \leq x \leq 1$ )	157
4.7.4	Summary	160
<b>CHAPTER 5 : CONCLUSIONS AND FUTURE OUTLOOK</b>		<b>161</b>
5.1	Conclusions	161
5.2	Future Outlook	165
<b>REFERENCES</b>		<b>166</b>
<b>APPENDICES</b>		<b>187</b>
<b>LIST OF PUBLICATION</b>		<b>196</b>

## LIST OF TABLES

NO.	PAGE
Table 1.1: Most common anode materials used for lithium ion batteries (Goriparti <i>et al.</i> , 2014).	9
Table 1.2: Characteristics of representative intercalation cathode compounds; crystal structure, theoretical/experimental/commercial capacity, average potentials and level of development (Nitta, Wu, Lee, & Yushin, 2014).	11
Table 2.1: Lattice constants reported in the literatures for LiMnPO <sub>4</sub> .	41
Table 2.2: Lattice constants reported in the literatures for LiCoPO <sub>4</sub> (Brutti & Panero, 2013).	44
Table 2.3: Lattice constants reported in the literatures for LiNiPO <sub>4</sub> .	46
Table 3.1: Summary of the synthesis conditions for the compositions prepared by solid state reaction method.	57
Table 3.2: Impedance parameters (Karthickprabhu, 2015).	67
Table 4.1: Refined structural parameters of LiCoPO <sub>4</sub> powders synthesised between 700 – 1000 °C for 12 hours in air.	78
Table 4.2: Initial model of LiCoPO <sub>4</sub> from ICSD data (#247497) (Koleva <i>et al.</i> , 2010)	80
Table 4.3: Refined structural parameters of LiMnPO <sub>4</sub> , LiCoPO <sub>4</sub> , and LiNiPO <sub>4</sub> compounds heated at 1000 °C for 12 hours in air.	83
Table 4.4: Summary of <i>dc</i> conductivities and activation energies of LiMPO <sub>4</sub> ( <i>M</i> = Mn, Co, Ni).	85
Table 4.5: Refined structural parameters of LiCo <sub>1-x</sub> [Ni <sub>0.5</sub> Mn <sub>0.5</sub> ] <sub>x</sub> PO <sub>4</sub> (0 ≤ <i>x</i> ≤ 1) heated at 1000 °C for 12 hours then slowly cooled to room temperature.	91
Table 4.6: Refined structural parameters of LiCo <sub>1-x</sub> [Ni <sub>0.5</sub> Mn <sub>0.5</sub> ] <sub>x</sub> PO <sub>4</sub> (0 ≤ <i>x</i> ≤ 1) heated at 1000 °C for 12 hours then quenched to room temperature.	91
Table 4.7: Summary of anti-site defects, crystallite size and lattice strain of LiCo <sub>1-x</sub> [Ni <sub>0.5</sub> Mn <sub>0.5</sub> ] <sub>x</sub> PO <sub>4</sub> (0 ≤ <i>x</i> ≤ 1).	92
Table 4.8: Summary of <i>dc</i> conductivities and activation energies of LiCo <sub>1-x</sub> [Ni <sub>0.5</sub> Mn <sub>0.5</sub> ] <sub>x</sub> PO <sub>4</sub> (0 ≤ <i>x</i> ≤ 1).	98

Table 4.9:	Refined structural parameters of $\text{LiNi}_{1-x}[\text{Co}_{0.5}\text{Mn}_{0.5}]_x\text{PO}_4$ ( $0 \leq x \leq 1$ ) heated at 1000 °C for 12 hours then slowly cooled to room temperature.	109
Table 4.10:	Refined structural parameters of $\text{LiNi}_{1-x}[\text{Co}_{0.5}\text{Mn}_{0.5}]_x\text{PO}_4$ ( $0 \leq x \leq 1$ ) heated at 1000 °C for 12 hours then quenched to room temperature.	109
Table 4.11:	Summary of anti-site defects, crystallite size and lattice strain of $\text{LiNi}_{1-x}[\text{Co}_{0.5}\text{Mn}_{0.5}]_x\text{PO}_4$ ( $0 \leq x \leq 1$ ).	109
Table 4.12:	Summary of <i>dc</i> conductivities and activation energies of $\text{LiNi}_{1-x}[\text{Co}_{0.5}\text{Mn}_{0.5}]_x\text{PO}_4$ ( $0 \leq x \leq 0.8$ ).	117
Table 4.13:	Refined structural parameters of $\text{LiMn}_{1-x}[\text{Co}_{0.5}\text{Ni}_{0.5}]_x\text{PO}_4$ ( $0 \leq x \leq 1$ ) heated at 1000 °C for 12 hours then slowly cooled to room temperature.	126
Table 4.14:	Refined structural parameters of $\text{LiMn}_{1-x}[\text{Co}_{0.5}\text{Ni}_{0.5}]_x\text{PO}_4$ ( $0 \leq x \leq 1$ ) heated at 1000 °C for 12 hours then quenched to room temperature.	126
Table 4.15:	Summary of anti-site defects, crystallite size and lattice strain of $\text{LiMn}_{1-x}[\text{Co}_{0.5}\text{Ni}_{0.5}]_x\text{PO}_4$ ( $0 \leq x \leq 1$ ).	128
Table 4.16:	Summary of <i>dc</i> conductivities and activation energies of $\text{LiMn}_{1-x}[\text{Co}_{0.5}\text{Ni}_{0.5}]_x\text{PO}_4$ ( $0 \leq x \leq 1$ ).	133
Table 4.17:	Refined structural parameters of $\text{LiNi}_{1/3}\text{Mn}_{1/3}\text{Co}_{1/3}\text{PO}_4$ synthesised at 700-1000 °C for 12 hours in air obtained by Rietveld refinements.	139
Table 4.18:	Refined structural parameters of $\text{LiNi}_{1/3}\text{Mn}_{1/3}\text{Co}_{1/3}\text{PO}_4$ synthesised at 800 °C for 12 hours in air obtained by Rietveld refinements.	146
Table 4.19:	The values of $\beta$ (full-width-half-maximum) and the calculated crystallite size of the five most intense reflection plane for non-milled sample and the samples milled for 8, 16 and 24 hours, respectively.	147
Table 4.20:	Impedance parameters derived from experimental Nyquist plots of $\text{LiNi}_{1/3}\text{Mn}_{1/3}\text{Co}_{1/3}\text{PO}_4$ @C/Li cells fitted by equivalent circuit Model A.	151
Table 4.21:	Impedance parameters derived from experimental Nyquist plots of $\text{LiNi}_{1/3}\text{Mn}_{1/3}\text{Co}_{1/3}\text{PO}_4$ @C/Li cells fitted by equivalent circuit Model B.	151
Table 4.22:	Refined structural parameters, unit cell volume and crystallite size of $\text{Li}_2\text{Co}_{1-x}\text{Zn}_x\text{Mn}_3\text{O}_8$ ( $0 \leq x \leq 1.0$ ).	156

Table 5.1:	Structural properties of the three series $\text{LiCo}_{1-x}[\text{Ni}_{0.5}\text{Mn}_{0.5}]_x\text{PO}_4$ , $\text{LiNi}_{1-x}[\text{Co}_{0.5}\text{Mn}_{0.5}]_x\text{PO}_4$ , and $\text{LiMn}_{1-x}[\text{Co}_{0.5}\text{Ni}_{0.5}]_x\text{PO}_4$ ( $0 \leq x \leq 1$ ) compositions.	163
Table A1:	Example of calculation of mass needed to prepare 6 g of $\text{LiNi}_{1/3}\text{Mn}_{1/3}\text{Co}_{1/3}\text{PO}_4$ powder.	187
Table A2:	Structural parameters of $\text{LiCo}_{1-x}[\text{Ni}_{0.5}\text{Mn}_{0.5}]_x\text{PO}_4$ ( $0 \leq x \leq 1$ ) heated at 1000 °C for 12 hours then slow-cooled to room temperature.	188
Table A3:	Structural parameters of $\text{LiCo}_{1-x}[\text{Ni}_{0.5}\text{Mn}_{0.5}]_x\text{PO}_4$ ( $0 \leq x \leq 1$ ) heated at 1000 °C for 12 hours then quenched to room temperature.	189
Table A4:	Structural parameters of $\text{LiNi}_{1-x}[\text{Co}_{0.5}\text{Mn}_{0.5}]_x\text{PO}_4$ ( $0 \leq x \leq 1$ ) heated at 1000 °C for 12 hours then slow-cooled to room temperature.	190
Table A5:	Structural parameters of $\text{LiNi}_{1-x}[\text{Co}_{0.5}\text{Mn}_{0.5}]_x\text{PO}_4$ ( $0 \leq x \leq 1$ ) heated at 1000 °C for 12 hours then quenched to room temperature.	191
Table A6:	Structural parameters of $\text{LiMn}_{1-x}[\text{Co}_{0.5}\text{Ni}_{0.5}]_x\text{PO}_4$ ( $0 \leq x \leq 1$ ) heated at 1000 °C for 12 hours then slow-cooled to room temperature.	192
Table A7:	Structural parameters of $\text{LiMn}_{1-x}[\text{Co}_{0.5}\text{Ni}_{0.5}]_x\text{PO}_4$ ( $0 \leq x \leq 1$ ) heated at 1000 °C for 12 hours then quenched to room temperature.	193
Table A8:	Structural parameters of $\text{LiNi}_{1/3}\text{Mn}_{1/3}\text{Co}_{1/3}\text{PO}_4$ heated at 700-1000 °C for 12 hours.	194
Table A9:	Detailed refined structural parameters of $\text{LiNi}_{1/3}\text{Mn}_{1/3}\text{Co}_{1/3}\text{PO}_4$ that were ball milled for 8, 16 and 24 hours, respectively.	195

## LIST OF FIGURES

NO.	PAGE
Figure 1.1: Comparison between different battery technologies in term of volumetric and gravimetric energy densitites (Tarascon & Armand, 2001).	2
Figure 1.2: Schematic of (a) heat quality (b) energy quality, showing analogous to the concept of heat quality, in which high voltage energy similar to high-temperature heat can be more useful. (c) Comparison between several high energy quality of cathodes and anodes (Shi <i>et al.</i> , 2018).	3
Figure 1.3: A schematic diagram illustrating the operating principle of a $\text{Li}_x\text{C}_6 / \text{Li}_{1-x}\text{Ni}_x\text{PO}_4$ lithium-ion cell during discharging and charging (Rommel <i>et al.</i> , 2014).	4
Figure 1.4: Crystal structures of (a) lithiated graphite (Yamada <i>et al.</i> , 2014), (b) lithium titanate (LTO) (Teshima <i>et al.</i> , 2011), and (c) silicon during lithiation (Chan, Wolverton, & Greeley, 2012).	6
Figure 1.5: Ternary phase diagram of $\text{LiCoPO}_4 - \text{LiNiPO}_4 - \text{LiMnPO}_4$ solid solution system. The compositions studied are indicated by red closed circles.	17
Figure 2.1: Crystal structure of three main cathode compounds illustrating the diffusion of $\text{Li}^+$ ions through the 2-D (layered), 3-D (spinel) and 1-D (olivine) frameworks (Julien <i>et al.</i> , 2014).	20
Figure 2.2: Layered $\alpha\text{-NaFeO}_2$ type structure $\text{LiMO}_2$ ( $M$ = most transition metals, such as Co, Mn, Ni, etc.) viewed along the a-axis. Green, blue and red represent Li, $M$ and O, respectively. (Reproduced using VESTA, source: Whittingham, 2004).	22
Figure 2.3: Spinel structure of $\text{LiMn}_2\text{O}_4$ . Green, pink and red represent Li, Mn and O, respectively. (Reproduced using VESTA, source: Wang, 2015).	22
Figure 2.4: Crystal structure of olivine $\text{LiMPO}_4$ ( $M = \text{Fe, Mn, Co, and Ni}$ ) viewed along the b-axis. Green, blue, violet and red represent Li, Co, P and O, respectively (Reproduced using VESTA, source: West, 2014).	23
Figure 2.5: Voltage and capacity ranges of the most popular cathode materials for Li-ion batteries. (Reproduced from Julien & Mauger, 2013)	25
Figure 2.6: The variations of discharge capacity with cycle number for $\text{Li}(\text{Mn}_{2-x}\text{Co}_x)\text{O}_4$ ( $0 \leq x \leq 0.5$ ) cell with 1M $\text{LiPF}_6$ in EC(1):DMC(2) electrolyte at room temperature (Shen <i>et al.</i> , 2001).	31

Figure 2.7: Slow scan cyclic voltammetry (20 $\mu\text{V/s}$ ) of three Zn-doped materials with Zn composition of $x =$ (a) 0.0 (b) 0.25, and (c) 0.5 in $\text{LiZn}_x\text{Mn}_{2-x}\text{O}_4$ . Li metal served as anode and reference electrodes (Ein-Eli <i>et al.</i> , 2005).	32
Figure 2.8: X-ray patterns of ordered ( $P4_332$ ) and disordered ( $Fd-3m$ ) spinel $\text{LiNi}_{0.5}\text{Mn}_{1.5}\text{O}_4$ (Manthiram <i>et al.</i> , 2014).	35
Figure 2.9: Discharge curves of the $\text{LiFePO}_4$ prepared from a composite of the phosphate with a carbon xerogel at different rates (Huang <i>et al.</i> , 2001).	36
Figure 2.10: Relative energy levels of the $M^{3+}/M^{2+}$ redox couple vs. $\text{Li/Li}^+$ in different $\text{LiMPO}_4$ ( $M = \text{Fe, Mn, Co and Ni}$ ) (Rommel <i>et al.</i> , 2014).	39
Figure 2.11: XRD patterns of the $\text{LiMPO}_4$ ( $M = \text{Mn, Fe, Co, Ni}$ ) samples prepared by the microwave assisted-solvothermal method (MW-ST) within 5 to 15 min at 300 $^\circ\text{C}$ (Murugan <i>et al.</i> , 2009).	39
Figure 2.12: XRD patterns of $\text{LiMPO}_4$ ( $M = \text{Mn, Co, and Ni}$ ) compounds synthesized by solid-state chemical reaction (Julien <i>et al.</i> , 2006).	47
Figure 2.13: The electrical conductivity and activation energy, $E_a$ in eV of $\text{LiMPO}_4$ ( $M = \text{Fe, Mn, Co, Ni}$ ) olivine materials (Zaghib, Mauger, & Julien, 2015).	48
Figure 2.14: The changes in cell voltage and specific capacity on different metal ion complex (Kandhasamy, Nallathamby, & Minakshi, 2012).	49
Figure 3.1: Flow chart illustrating the simplified research methodology in this research.	53
Figure 3.2: Schematic diagram of typical solid state reaction method.	55
Figure 3.3: (a) Schematic illustration of the geometry used for the simplified derivation of Bragg's law for a set of given crystal planes. (b) Schematic diagram of a powder X-ray diffraction experiment with the Bragg-Brentano setup (Ellis, 2013).	60
Figure 3.4: The construction of coin cells.	70
Figure 3.5: (a) Typical complex-plane or Nyquist plot for the impedance spectrum of (b) simple parallel RC equivalent circuit, showing top-point characteristic frequency $\omega = 1/RC$ (Barsoukov & Macdonald, 2005).	71
Figure 3.6: (a) The Nyquist plot and (b) the equivalent circuit of simplified Randle's cell (Gamry instrument, 2017).	72
Figure 4.1: Normalised XRD patterns of $\text{LiCoPO}_4$ powders synthesised between 700 and 1000 $^\circ\text{C}$ for 12 hours in air.	76

Figure 4.2:	Indexed XRD pattern for $\text{LiCoPO}_4$ powder synthesised at $850\text{ }^\circ\text{C}$ for 12 hours in air.	76
Figure 4.3:	The variations of lattice parameters of $\text{LiCoPO}_4$ as a function of temperature.	77
Figure 4.4:	(a) Normalized XRD patterns of $\text{LiMnPO}_4$ , $\text{LiCoPO}_4$ , and $\text{LiNiPO}_4$ synthesised at $1000\text{ }^\circ\text{C}$ for 12 hours. (b) Enlarged XRD patterns in $2\theta$ range $35\text{-}37.5^\circ$ .	79
Figure 4.5:	Conductivity vs. frequency spectra for (a) $\text{LiMnPO}_4$ , (b) $\text{LiCoPO}_4$ , and (c) $\text{LiNiPO}_4$ compounds heated at $1000\text{ }^\circ\text{C}$ for 12 hours in air.	85
Figure 4.6:	SEM images for (a) $\text{LiMnPO}_4$ , (b) $\text{LiCoPO}_4$ , and (c) $\text{LiNiPO}_4$ compounds heated at $1000\text{ }^\circ\text{C}$ for 12 hours in air.	86
Figure 4.7:	Normalized XRD patterns of $\text{LiCo}_{1-x}[\text{Ni}_{0.5}\text{Mn}_{0.5}]_x\text{PO}_4$ ( $0 \leq x \leq 1$ ) powders synthesised at $1000\text{ }^\circ\text{C}$ for 12 hours then slowly cooled in air.	88
Figure 4.8:	Normalized XRD patterns of $\text{LiCo}_{1-x}[\text{Ni}_{0.5}\text{Mn}_{0.5}]_x\text{PO}_4$ ( $0 \leq x \leq 1$ ) powders synthesised at $1000\text{ }^\circ\text{C}$ for 12 hours then quenched to room temperature.	89
Figure 4.9:	Enlarged XRD patterns of slow-cooled and quenched $\text{LiCo}_{1-x}[\text{Ni}_{0.5}\text{Mn}_{0.5}]_x\text{PO}_4$ ( $0 \leq x \leq 1$ ) in $2\theta$ range $35\text{-}37.8^\circ$ .	90
Figure 4.10:	The variations of lattice parameters $a$ , $b$ , $c$ and unit cell volume as a function of Co content.	92
Figure 4.11:	The estimated amount of anti-site defects in slow-cooled and quenched $\text{LiCo}_{1-x}[\text{Ni}_{0.5}\text{Mn}_{0.5}]_x\text{PO}_4$ ( $0 \leq x \leq 1$ ).	94
Figure 4.12:	Photographic image showing the physical colour of single phase $\text{LiCo}_{1-x}[\text{Ni}_{0.5}\text{Mn}_{0.5}]_x\text{PO}_4$ ( $0 \leq x \leq 1$ ) prepared at $850\text{ }^\circ\text{C}$ .	95
Figure 4.13:	Plots of the conductivity vs. frequency spectra for slow-cooled $\text{LiCo}_{1-x}[\text{Ni}_{0.5}\text{Mn}_{0.5}]_x\text{PO}_4$ ( $0 \leq x \leq 1$ ) as a function of temperature.	97
Figure 4.14:	Plots of the conductivity vs. frequency spectra for quenched $\text{LiCo}_{1-x}[\text{Ni}_{0.5}\text{Mn}_{0.5}]_x\text{PO}_4$ ( $0 \leq x \leq 1$ ) as a function of temperature.	98
Figure 4.15:	Arrhenius plots of the electrical conductivity of $\text{LiCo}_{1-x}[\text{Ni}_{0.5}\text{Mn}_{0.5}]_x\text{PO}_4$ ( $0 \leq x \leq 1$ ) for the calculation of activation energy, $E_a$ at temperature $200\text{-}350\text{ }^\circ\text{C}$ , (a) slow cooling (b) fast cooling.	99

Figure 4.16: SEM images of $\text{LiCo}_{1-x}[\text{Ni}_{0.5}\text{Mn}_{0.5}]_x\text{PO}_4$ ( $0 \leq x \leq 1$ ) pellets heated at 1000 °C for 12 hours in air.	102
Figure 4.17: Normalized XRD patterns of $\text{LiNi}_{1-x}[\text{Co}_{0.5}\text{Mn}_{0.5}]_x\text{PO}_4$ ( $0 \leq x \leq 1$ ) powders synthesised at 1000 °C for 12 hours then slowly cooled in air.	105
Figure 4.18: Normalized XRD patterns of $\text{LiNi}_{1-x}[\text{Co}_{0.5}\text{Mn}_{0.5}]_x\text{PO}_4$ ( $0 \leq x \leq 1$ ) powders synthesised at 1000 °C for 12 hours then quenched to room temperature.	106
Figure 4.19: Enlarged XRD patterns of slow-cooled and quenched $\text{LiNi}_{1-x}[\text{Co}_{0.5}\text{Mn}_{0.5}]_x\text{PO}_4$ ( $0 \leq x \leq 1$ ) in $2\theta$ range 35-37.8°.	107
Figure 4.20: The variations of lattice parameters $a$ , $b$ , $c$ and unit cell volume as a function of Ni content.	110
Figure 4.21: The estimated amount of anti-site defects in slow-cooled and quenched $\text{LiNi}_{1-x}[\text{Co}_{0.5}\text{Mn}_{0.5}]_x\text{PO}_4$ ( $0 \leq x \leq 1$ ).	112
Figure 4.22: Photographic image showing the physical colour of single phase $\text{LiNi}_{1-x}[\text{Co}_{0.5}\text{Mn}_{0.5}]_x\text{PO}_4$ ( $0 \leq x \leq 1$ ) prepared at 850 °C.	113
Figure 4.23: Plots of the conductivity vs. frequency spectra for slow-cooled $\text{LiNi}_{1-x}[\text{Co}_{0.5}\text{Mn}_{0.5}]_x\text{PO}_4$ ( $0 \leq x \leq 0.8$ ) as a function of temperature.	115
Figure 4.24: Plots of the conductivity vs. frequency spectra for quenched $\text{LiNi}_{1-x}[\text{Co}_{0.5}\text{Mn}_{0.5}]_x\text{PO}_4$ ( $0 \leq x \leq 0.8$ ) as a function of temperature.	116
Figure 4.25: Arrhenius plots of the electrical conductivity of $\text{LiNi}_{1-x}[\text{Co}_{0.5}\text{Mn}_{0.5}]_x\text{PO}_4$ ( $0 \leq x \leq 0.8$ ) for the calculation of activation energy, $E_a$ at temperature 200-350 °C, (a) slow cooling (b) fast cooling.	118
Figure 4.26: SEM images of $\text{LiNi}_{1-x}[\text{Co}_{0.5}\text{Mn}_{0.5}]_x\text{PO}_4$ ( $0 \leq x \leq 1$ ) pellets heated at 1000 °C for 12 hours in air.	120
Figure 4.27: Normalized XRD patterns of $\text{LiMn}_{1-x}[\text{Co}_{0.5}\text{Ni}_{0.5}]_x\text{PO}_4$ ( $0 \leq x \leq 1$ ) powders synthesised at 1000 °C for 12 hours then slowly cooled in air.	123
Figure 4.28: Normalized XRD patterns of $\text{LiMn}_{1-x}[\text{Co}_{0.5}\text{Ni}_{0.5}]_x\text{PO}_4$ ( $0 \leq x \leq 1$ ) powders synthesised at 1000 °C for 12 hours then quenched to room temperature.	124
Figure 4.29: Enlarged XRD patterns of slow-cooled and quenched $\text{LiMn}_{1-x}[\text{Co}_{0.5}\text{Ni}_{0.5}]_x\text{PO}_4$ ( $0 \leq x \leq 1$ ) in $2\theta$ range 35-37.8°.	125

Figure 4.30: The variations of lattice parameters $a$ , $b$ , $c$ and unit cell volume as a function of Mn content.	127
Figure 4.31: The estimated amount of anti-site defects in slow-cooled and quenched $\text{LiMn}_{1-x}[\text{Co}_{0.5}\text{Ni}_{0.5}]_x\text{PO}_4$ ( $0 \leq x \leq 1$ ).	129
Figure 4.32: Photographic image showing the physical colour of single phase $\text{LiMn}_{1-x}[\text{Co}_{0.5}\text{Ni}_{0.5}]_x\text{PO}_4$ ( $0 \leq x \leq 1$ ) prepared at 850 °C.	130
Figure 4.33: Plots of the conductivity vs. frequency spectra for slow-cooled $\text{LiMn}_{1-x}[\text{Co}_{0.5}\text{Ni}_{0.5}]_x\text{PO}_4$ ( $0 \leq x \leq 1$ ) as a function of temperature.	131
Figure 4.34: Plots of the conductivity vs. frequency spectra for quenched $\text{LiMn}_{1-x}[\text{Co}_{0.5}\text{Ni}_{0.5}]_x\text{PO}_4$ ( $0 \leq x \leq 1$ ) as a function of temperature.	132
Figure 4.35: Arrhenius plots of the electrical conductivity of $\text{LiMn}_{1-x}[\text{Co}_{0.5}\text{Ni}_{0.5}]_x\text{PO}_4$ ( $0 \leq x \leq 1$ ) for the calculation of activation energy, $E_a$ at temperature 200-350 °C, (a) slow cooling (b) fast cooling.	133
Figure 4.36: SEM images of $\text{LiMn}_{1-x}[\text{Co}_{0.5}\text{Ni}_{0.5}]_x\text{PO}_4$ ( $0 \leq x \leq 1$ ) pellets heated at 1000 °C for 12 hours in air.	134
Figure 4.37: Normalised XRD patterns of $\text{LiNi}_{1/3}\text{Mn}_{1/3}\text{Co}_{1/3}\text{PO}_4$ synthesised between 700 and 1000 °C for 12 hours in air.	138
Figure 4.38: The variations of structural parameters $a$ , $b$ , $c$ and unit cell volume as a function of temperature.	139
Figure 4.39: The estimated amount of anti-site defects estimated from Rietveld refinements as a function of temperature.	140
Figure 4.40: Conductivity vs. frequency spectra for $\text{LiNi}_{1/3}\text{Mn}_{1/3}\text{Co}_{1/3}\text{PO}_4$ sintered at (a) 800 °C (b) 1000 °C for 12 hours.	141
Figure 4.41: Arrhenius plots of the electrical conductivity of at the frequency of 1k Hz for the calculation of activation energy, $E_a$ at temperatures between 200 °C and 350 °C.	142
Figure 4.42: SEM images of $\text{LiNi}_{1/3}\text{Mn}_{1/3}\text{Co}_{1/3}\text{PO}_4$ pellets heated between 700 °C and 1000 °C for 12 hours in air.	143
Figure 4.43: (a) Normalised XRD patterns of $\text{LiNi}_{1/3}\text{Mn}_{1/3}\text{Co}_{1/3}\text{PO}_4$ synthesised at 800 °C followed by different ball milling time. (b) Enlarged XRD patterns of in the $2\theta$ range of 35 to 41°.	144
Figure 4.44: The variations of structural parameters $a$ , $b$ , $c$ and unit cell volume as a function of ball milling time.	146

- Figure 4.45: Nyquist plots ( $Z'$  vs.  $-Z''$ ) from EIS spectra of  $\text{LiNi}_{1/3}\text{Mn}_{1/3}\text{Co}_{1/3}\text{PO}_4@C/\text{Li}$  cells. Experimental spectra are represented by symbols and fitted data using (a) and (b) Model A, (c) and (d) Model B are represented by continuous lines. 149
- Figure 4.46: Physical equivalent circuit Model A and Model B that were used to describe EIS data. 150
- Figure 4.47: XRD patterns of  $\text{Li}_2\text{Co}_{1-x}\text{Zn}_x\text{Mn}_3\text{O}_8$  ( $0 \leq x \leq 1.0$ ) compounds that were synthesised at  $800^\circ\text{C}$ . 154
- Figure 4.48: The variations of structural parameters  $a$  and unit cell volume as a function of Zn content. 155
- Figure 4.49: SEM images of  $\text{Li}_2\text{Co}_{1-x}\text{Zn}_x\text{Mn}_3\text{O}_8$  ( $0 \leq x \leq 1$ ) compounds at magnification of  $5000\times$ . 157
- Figure 4.50: The galvanostatic charge-discharge profile for 1st, 2nd, and 50th cycle of  $\text{Li}_2\text{Co}_{1-x}\text{Zn}_x\text{Mn}_3\text{O}_8$  ( $0 \leq x \leq 1$ ) compounds that were synthesised at  $800^\circ\text{C}$ . 158
- Figure 4.51: The discharge capacities vs cycle number plots of  $\text{Li}_2\text{Co}_{1-x}\text{Zn}_x\text{Mn}_3\text{O}_8$  ( $0 \leq x \leq 1$ ) compounds that were synthesised at  $800^\circ\text{C}$ . 159

## LIST OF ABBREVIATIONS

CPE	Constant Phase Element
DEC	Diethyl Carbonate
DMC	Dimethyl Carbonate
EIS	Electrochemical Impedance Spectroscopy
EC	Ethylene Carbonate
FWHM	Full Width Half Maximum
GSAS	General Structure Analysis System
HEV	Hybrid Electric Vehicles
ICSD	Inorganic Crystal Structure Database
ICDD	International Center for Diffraction Data
JCPDS	Joint Committee for Powder Diffraction Studies
LIB	Lithium-ion batteries
PVDF	Poly (Vinylidene fluoride)
PDF	Powder Diffraction File
PC	Propylene Carbonate
SEM	Scanning electron microscopy
VESTA	Visualization for Electronic and Structural Analysis
XRD	X-ray diffraction

## LIST OF SYMBOLS

$E_a$	Activation energy
$Y$	Admittance
$\omega$	Angular frequency
$k$	Boltzmann's Constant
$Q$	Charge
$R_{ct}$	Charge transfer resistance
$L$	Crystallite size
$^{\circ}C$	Degree celsius
$\theta$	Diffraction angle
$\sigma$	Electrical conductivity
$\beta$	Full Width Half Maximum
$h$	Hours
$Z''$	Imaginary part of Impedance
$d$	Interplanar spacing
$\varepsilon$	Lattice strain
$Z'$	Real part of Impedance
$S$	Siemens
$V$	Voltage
$\lambda$	Wavelength of X-rays

## LIST OF EQUATIONS

NO.		PAGE
1.1	Anode: $C + xLi + xe^- \leftrightarrow Li_xC_6$	4
1.2	Cathode: $LiCoO_2 \leftrightarrow Li_{1-x}CoO_2 + xLi + xe^-$	4
2.1	$Li_{Li^x} + M_{M^x} \rightarrow Li_{M'} + M_{Li^\circ}$	50
3.1	$n \lambda = 2 d_{hkl} \sin \theta_{hkl}$	59
3.2	$\beta = \frac{k\lambda}{L \cos \theta}$	60
3.3	$\beta = 4\varepsilon \frac{\sin \theta}{\cos \theta} = 4\varepsilon \tan \theta$	61
3.4	$\beta = \frac{k\lambda}{L \cos \theta} + 4\varepsilon \frac{\sin \theta}{\cos \theta}$	61
3.5	$\beta^2 \cos^2 \theta = 16\varepsilon^2 \sin^2 \theta + \frac{k^2 \lambda^2}{L^2}$	61
3.6	Gaussian component: $FWHM = (U \tan^2 \theta + V \tan \theta + W)^{1/2}$	64
3.7	Lorentzian component: $FWHM = (X \tan \theta + Y / \cos \theta)^{1/2}$	64
3.8	$\chi^2 = \left( \frac{R_{wp}}{R_{exp}} \right)^2$	65
3.9	$Z^* = \frac{1}{Y^*} = Z' + jZ''$	66
3.10	$\varepsilon^* = \frac{1}{M^*}$	66
3.11	$M^* = j\omega C_0 Z^*$	66
3.12	$\varepsilon^* = \frac{Y^*}{j\omega C_0 Z^*}$	66
3.13	$M^* = \frac{1}{\varepsilon^*} = j\omega C_0 Z^* = \frac{j\omega C_0}{Y^*}$	66
3.14	$\sigma = \frac{1}{R} \times \frac{l}{A}$	67
3.15	$\sigma T = \sigma_0 e^{\frac{-E_a}{kT}}$	68
3.16	$\omega_{max} = 2\pi f_{max} = (RC)^{-1} = \tau^{-1}$	71
3.17	$Z''_{max} = \frac{R}{2}$	71

3.18	$Q = I \times t$	73
4.1	$\sigma(\omega) = \sigma_{dc} + A\omega^n$	84

©This item is protected by original copyright

## Sintesis dan Pencirian Bahan Katod dalam Fasa Segitiga LiCoPO<sub>4</sub>-LiNiPO<sub>4</sub>-LiMnPO<sub>4</sub> untuk Bateri Lithium Ion

### ABSTRAK

Peranti penyimpanan tenaga elektrokimia dengan ketumpatan tenaga yang tinggi adalah penting dalam masyarakat moden. Bahan katod yang mempunyai voltan nyahcas dan kapasiti nyahcas yang tinggi diperlukan untuk mendapatkan bateri litium yang mempunyai ketumpatan tenaga yang tinggi. Oleh itu, bahan katod voltan tinggi seperti olivine LiMPO<sub>4</sub> ( $M = \text{Mn, Co, and Ni}$ ) dan spinel Li<sub>2</sub>CoMn<sub>3</sub>O<sub>8</sub> telah dikaji secara meluas oleh penyelidik-penyelidik. Dalam kajian ini, tiga siri analog dengan formula LiCo<sub>1-x</sub>[Ni<sub>0.5</sub>Mn<sub>0.5</sub>]<sub>x</sub>PO<sub>4</sub>, LiNi<sub>1-x</sub>[Co<sub>0.5</sub>Mn<sub>0.5</sub>]<sub>x</sub>PO<sub>4</sub> dan LiMn<sub>1-x</sub>[Co<sub>0.5</sub>Ni<sub>0.5</sub>]<sub>x</sub>PO<sub>4</sub> ( $0 \leq x \leq 1$ ) yang berstruktur olivine dalam fasa segitiga LiCoPO<sub>4</sub> – LiNiPO<sub>4</sub> – LiMnPO<sub>4</sub> telah dikaji secara sistematik sebagai calon berpotensi untuk bateri litium cas semul yang beroperasi pada voltan tinggi. Sampel-sampel telah disediakan melalui kaedah sintesis keadaan pepejal konvensional. Semua sampel telah dipanaskan pada suhu 750–1000 °C dalam udara selama 12 jam dengan dua pendekatan pendinginan yang berbeza, iaitu pendinginan perlahan dan pelindapkejutan. Pencirian komposisi-komposisi ini telah dilakukan dengan menggunakan Pembelauan sinar-X (XRD), Mikroskop Imbasan Elektron (SEM) dan Analisis Impedans Spektroskopi. Pada mulanya, LiCoPO<sub>4</sub>, LiNiPO<sub>4</sub> dan LiMnPO<sub>4</sub> telah disintesis dan telah digunakan sebagai rujukan piawai. Analisis XRD menunjukkan bahawa semua sampel yang disintesis telah mencapai fasa tulen dan kestabilan struktur sehingga suhu 1000 °C. Semua sampel mempunyai struktur olivine dengan kumpulan ruang *Pnma*. Analisis struktur yang menggunakan kaedah penyaringan Rietveld menggunakan data XRD konvensional telah mendedahkan bahawa anggaran jumlah kecacatan kekisi (*anti-site*) adalah rendah iaitu kurang daripada ~ 5%. Perubahan parameter kekisi bagi sampel ketiga-tiga siri adalah selaras dengan hukum Vegard. Perbandingan struktur dan sifat elektrik antara sampel yang dilindapkejut dengan sampel yang didinginkan dengan perlahan telah dilakukan. Keputusan menunjukkan bahawa jumlah kecacatan kekisi (*anti-site*) dalam kedua-dua kaedah pendinginan mempunyai nilai yang lebih kurang sama. Walau bagaimanapun, semua sampel menunjukkan sifat keberaliran elektrik hakiki yang rendah iaitu sekitar 10<sup>-8</sup> S cm<sup>-1</sup> apabila diukur dengan LCR meter pada suhu 300 °C. Oleh itu, kajian lanjut telah dilakukan pada LiNi<sub>1/3</sub>Mn<sub>1/3</sub>Co<sub>1/3</sub>PO<sub>4</sub> untuk meningkatkan kekonduksiannya. LiNi<sub>1/3</sub>Mn<sub>1/3</sub>Co<sub>1/3</sub>PO<sub>4</sub> telah diproses dengan menggunakan kaedah pengisaran bebola untuk mengurangkan saiz zarah. Selepas itu, LiNi<sub>1/3</sub>Mn<sub>1/3</sub>Co<sub>1/3</sub>PO<sub>4</sub> telah dicampur dengan pelbagai bahan bersumber karbon: graphene nano-platelets (GNP), nanotub karbon (CNT) and hitam karbon (CB) untuk membentuk komposit. Keputusan menunjukkan bahawa komposit-komposit LiNi<sub>1/3</sub>Mn<sub>1/3</sub>Co<sub>1/3</sub>PO<sub>4</sub>/C mempunyai kekonduksian yang lebih tinggi berbanding dengan LiNi<sub>1/3</sub>Mn<sub>1/3</sub>Co<sub>1/3</sub>PO<sub>4</sub> yang tanpa pengubahsuaian. Oleh itu, pengubahsuaian melalui pemprosesan tersebut berkemungkinan boleh digunakan untuk meningkatkan kekonduksian ketiga-tiga siri analog tersebut. Selain itu, satu lagi penyelidikan sampingan turut dijalankan untuk mengkaji kesan penggantian Zn dalam Li<sub>2</sub>CoMn<sub>3</sub>O<sub>8</sub>, walau bagaimanapun, hasilnya tidak begitu memuaskan kerana sampel yang mengandungi Zn menunjukkan kapasiti nyahcas yang rendah.

## Synthesis and Characterisation of Ternary System $\text{LiCoPO}_4\text{--LiNiPO}_4\text{--LiMnPO}_4$ Cathode Materials for Li-ion Batteries

### ABSTRACT

Electrochemical energy storage devices with high energy density are important in modern society. In order to obtain high energy density Li ion batteries, cathode materials with high discharge voltage and discharge capacity are required. Hence, high voltage cathode materials such as olivine  $\text{LiMPO}_4$  ( $M = \text{Mn, Co, and Ni}$ ) and spinel  $\text{Li}_2\text{CoMn}_3\text{O}_8$  have been extensively studied by researchers. In this study, three analogous series with the formula of  $\text{LiCo}_{1-x}[\text{Ni}_{0.5}\text{Mn}_{0.5}]_x\text{PO}_4$ ,  $\text{LiNi}_{1-x}[\text{Co}_{0.5}\text{Mn}_{0.5}]_x\text{PO}_4$  and  $\text{LiMn}_{1-x}[\text{Co}_{0.5}\text{Ni}_{0.5}]_x\text{PO}_4$  ( $0 \leq x \leq 1$ ) within the phase triangle of  $\text{LiCoPO}_4\text{--LiNiPO}_4\text{--LiMnPO}_4$  were systematically studied as potential candidates for high voltage rechargeable lithium ion batteries. The samples were synthesized by conventional solid state route at temperature  $750\text{--}1000\text{ }^\circ\text{C}$  in air for 12 hours with two different cooling conditions (i.e. slow cooling and quenching). These compositions were characterised by using X-ray Diffraction (XRD), Scanning Electron Microscopy (SEM) and Impedance Spectroscopy Analyser. Initially,  $\text{LiCoPO}_4$ ,  $\text{LiNiPO}_4$  and  $\text{LiMnPO}_4$  were prepared as end members and were used as standard references. The prepared samples were single phase and structurally stable up to  $1000\text{ }^\circ\text{C}$ . All the XRD patterns could be indexed with the olivine structure and the space group of  $Pnma$ . Structural analysis using Rietveld refinement of conventional XRD data revealed that the estimated anti-site defects was comparably low which is less than  $\sim 5\%$ . The changes in lattice parameters across the series Mn, Co and Ni were in accordance with Vegard's law. The structure and electrical properties of the slow-cooled and quenched samples were compared. The results showed that the anti-site defects in both the quench and slow-cooled samples have quite similar values. Nevertheless, all the samples exhibits low intrinsic electrical conductivities of about  $\sim 10^{-8}\text{ S cm}^{-1}$  that were measured using a LCR meter at  $300\text{ }^\circ\text{C}$ . Hence, further modification were performed on complex olivine  $\text{LiNi}_{1/3}\text{Mn}_{1/3}\text{Co}_{1/3}\text{PO}_4$  in order to improve the conductivity.  $\text{LiNi}_{1/3}\text{Mn}_{1/3}\text{Co}_{1/3}\text{PO}_4$  was ball milled to reduce the particle size followed by ball milling with three different carbon sources: graphene nano-platelets (GNP), carbon nanotube (CNT) and carbon black (CB) to form composites. The results showed that these composites have exhibited relatively higher coin cell conductivity compare to the bare sample. Hence, it was believed that this processing route can probably be applied to improve the conductivity of the three analogous series. On the other hand, a small research was also carried out to study the effect of Zn doped into spinel  $\text{Li}_2\text{CoMn}_3\text{O}_8$ , however, the result was not quite promising because the doped samples exhibited low discharge capacity.

## CHAPTER 1 : INTRODUCTION

### 1.1 Background

The research of lithium battery began in the 1950s, while research and development of the rechargeable Li-ion batteries (LIBs) began in the early 1980s at Asahi Chemicals (Brodd, 2009). LIBs have become a commercial reality in 1991 when the engineers from Sony managed to surprise the “battery world” by commercializing Li-ion battery (LIBs) which is based on a lithiated carbon anode and  $\text{LiCoO}_2$  as cathode. Since then, LIBs have been one of the most promising chemical-electrical energy conversion power sources owing to their outstanding properties which include higher energy density and operating voltage as compared to nickel metal hydride (Ni-MH) and lead acid batteries (Broussely, Biensan, & Simon, 1999). Diouf & Pode (2015) have disclosed the variety potential of the use of LIBs as primary energy storage substituting the very common lead acid batteries.

Figure 1.1 shows that LIBs are most suitable for consumer electronic devices because they are lighter and smaller than other rechargeable batteries for the same energy storage capacity. Nowadays, it is believed that the driving force for the development of LIBs in renewable energy sector could be the electric vehicle and the smart grid industry. Hence, improving the energy density of batteries is utmost urgent. Huggins (2009) introduced the concept of energy quality which can be defined as the amount of useful power or product that a unit energy can provide. In response to this concept, high voltage energy is similar to high temperature heat whereby it is often more useful as demonstrated in Figure 1.2a owing to the square relationship between the electrical power (P) and the

practical voltage (V) ( $P = V^2/R$ ). Hence, an ideal LIB must fulfil the requirement of high capacity and high operating voltage. In other words, both electrodes need to have high specific capacity besides having high discharge voltage for cathode materials and low charge voltage for anode materials (Fig. 1.2b). However, in reality, cathode materials usually have to compromise between the discharge voltage and the specific capacity. For example, it can be observed from Figure 1.2c,  $\text{LiNi}_{0.5}\text{Mn}_{1.5}\text{O}_4$  can achieve specific capacity of about  $120 \text{ mAh g}^{-1}$  when the discharge voltage is high ( $\sim 4.8 \text{ V}$ ) but  $\text{LiNi}_{0.8}\text{Mn}_{0.1}\text{Co}_{0.1}\text{O}_2$  can exhibit specific capacity above  $200 \text{ mAh g}^{-1}$  with intermediate discharge voltage of about  $3.6 \text{ V}$ . Nonetheless, there are many more issues to be concerned before the commercialization of LIB using these electrodes. The development of energy storage is a continuing challenge for researchers to pursue higher performance and to sustain the environment for future generations as well.

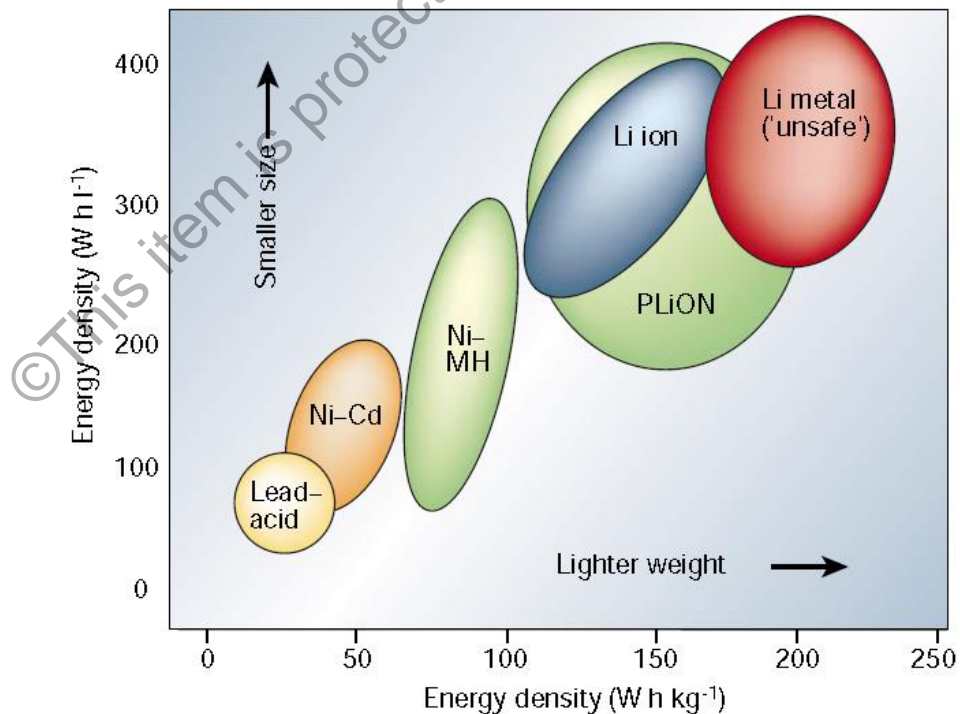


Figure 1.1: Comparison between different battery technologies in term of volumetric and gravimetric energy densities (Tarascon & Armand, 2001).

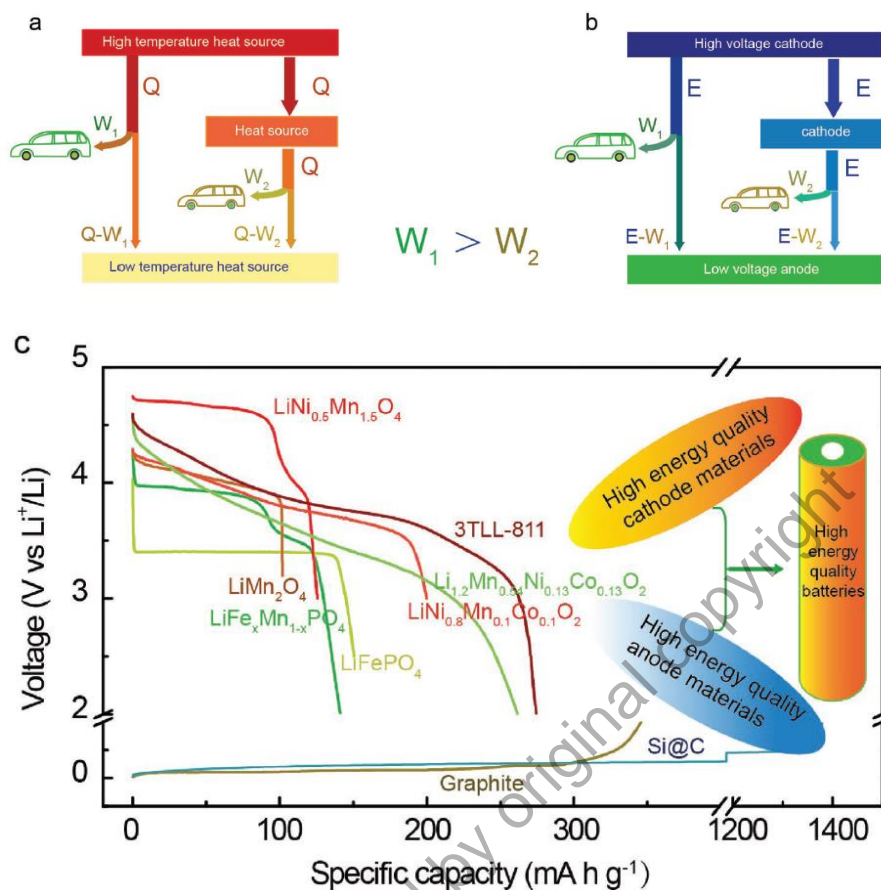


Figure 1.2: Schematic of (a) heat quality (b) energy quality, showing analogous to the concept of heat quality, in which high voltage energy similar to high-temperature heat can be more useful. (c) Comparison between several high energy quality of cathodes and anodes (Shi *et al.*, 2018).

### 1.1.1 Basic Operating Principle of Li-ion Batteries

In the most basic sense, a standard Li-ion battery usually refers to a battery which consists of cathode (positive electrode) and anode (negative electrode) materials serve as a host for the Li ions ( $\text{Li}^+$ ). The anode and cathode are separated by an ionically conductive but electronically insulating electrolyte, separator and current collector (mostly Al and Cu) as depicted in Figure 1.3 (Rommel, Schall, Brünig, & Wehrich, 2014). The common concept of present LIBs relies on transition metals oxides or phosphates ( $\text{LiCoO}_2$ ,  $\text{LiMn}_2\text{O}_4$ ,  $\text{LiCo}_{1/3}\text{Mn}_{1/3}\text{Ni}_{1/3}\text{O}_2$ ,  $\text{LiFePO}_4$ , etc.) as cathode active material, while graphite is commonly used as anode active material. A separator in